

Recovering fetal signals transabdominally through interferometric near-infrared spectroscopy (iNIRS): supplement

SHING-JIUAN LIU,¹ SU YEON LEE,² CHRISTOPHER PIVETTI,² EDWIN KULUBYA,² AIJUN WANG,^{2,3} DIANA L. FARMER,² SOHEIL GHIASI,¹ AND WEIJIAN YANG^{1,*} 

¹*Department of Electrical and Computer Engineering, University of California, Davis, Davis, CA 95616, USA*

²*Department of Surgery, University of California, Davis, Sacramento, CA 95817, USA*

³*Department of Biomedical Engineering, University of California, Davis, Davis, CA 95616, USA*

**wejyang@ucdavis.edu*

This supplement published with Optica Publishing Group on 31 October 2023 by The Authors under the terms of the [Creative Commons Attribution 4.0 License](#) in the format provided by the authors and unedited. Further distribution of this work must maintain attribution to the author(s) and the published article's title, journal citation, and DOI.

Supplement DOI: <https://doi.org/10.6084/m9.figshare.24306511>

Parent Article DOI: <https://doi.org/10.1364/BOE.500898>

Recovering fetal signals transabdominally through interferometric near-infrared spectroscopy (iNIRS)

SHING-JIUAN LIU¹, SU YEON LEE², CHRISTOPHER PIVETTI², EDWIN KULUBYA², AIJUN WANG^{2,3}, DIANA L. FARMER², SOHEIL GHASI¹, AND WEIJIAN YANG^{1,*}

¹ Department of Electrical and Computer Engineering, University of California, Davis, Davis, CA 95616, USA

² Department of Surgery, University of California, Davis, Sacramento, CA 95817, USA

³ Department of Biomedical Engineering, University of California, Davis, Davis, CA 95616, USA

*Corresponding author: weiyang@ucdavis.edu

Supplementary Information

1. Monte Carlo simulation in a maternal-fetal two-subject reflection model

To simulate the propagation of light in the intrapartum environment, we employed a simplified tissue model comprising several layers: two maternal layers (layer 1: maternal dermal and subdermal tissue; layer 2: uterine tissue), a layer for amniotic fluid (layer 3), and one fetal layer (layer 4: fetal scalp, fetal arterial tissue, fetal skull, and fetal brain). The physical and optical properties assigned to each layer and wavelength were derived from published studies that investigated these properties using both ex vivo and in vivo tissues (refer to Table 1 in the main article for details). Fetal depth varies among pregnant individuals. To account for this variation, ultrasound technology was utilized to estimate the minimum fetal to maternal skin distance and this distance was modeled as a linear regression function of maternal weight and gestational age [1]. By considering a range of maternal weights (from 50kg to 80kg) at a gestational age of 40 weeks, we computed the minimum fetal to maternal skin distance, using the equation in [1], which fell within the range of 1.7 cm to 4.1 cm. Throughout pregnancy, most women have the uterus thickness to be 1.1-1.2 cm, though some of them could have it as thick as 1.6 cm [2, 3]. Three tissue models enabled us to simulate and analyze light propagation in diverse intrapartum scenarios: small fetal depth (1.8 cm) with thin uterus thickness (0.7 cm) (Fig. S1a-c), average fetal depth (2.9 cm) with an average uterus thickness (1.15cm) (Fig. 3 in the main article), and large fetal depth (4 cm) with thick uterus thickness (1.6 cm) (Fig. S1d-f). The average fetal depth scenario is presented in the main article Section 3.1, and here we present the other two scenarios (Fig. S1). In all three scenarios, the trends observed for metrics $M_1 \sim M_6$ align with those presented in the main article Section 3.1. In the context of iNIRS, the flexibility to choose a small SD distance becomes valuable when the fetal signal strength (M_4) is more pronounced within a shorter SD distance (Fig. S1b and Fig. S1e). In such case, iNIRS outperformed CW-NIRS by achieving a higher fetal signal contrast (M_6) compared to CW-NIRS' fetal signal contrast (M_5) (Fig. S1c and Fig. S1f). When comparing the three scenarios (small, average, and large fetal depth) in those depicted in Fig. S1 and Fig. 3 in the main article, we found that as the fetal depth increased, the disparity between iNIRS' M_6 and CW-NIRS' M_5 increased, especially at a short SD distance. This is because a larger fetal depth would result in a stronger maternal signal and iNIRS measurement could selectively filter the maternal signal, so the advantage of iNIRS over CW-NIRS becomes more significant.

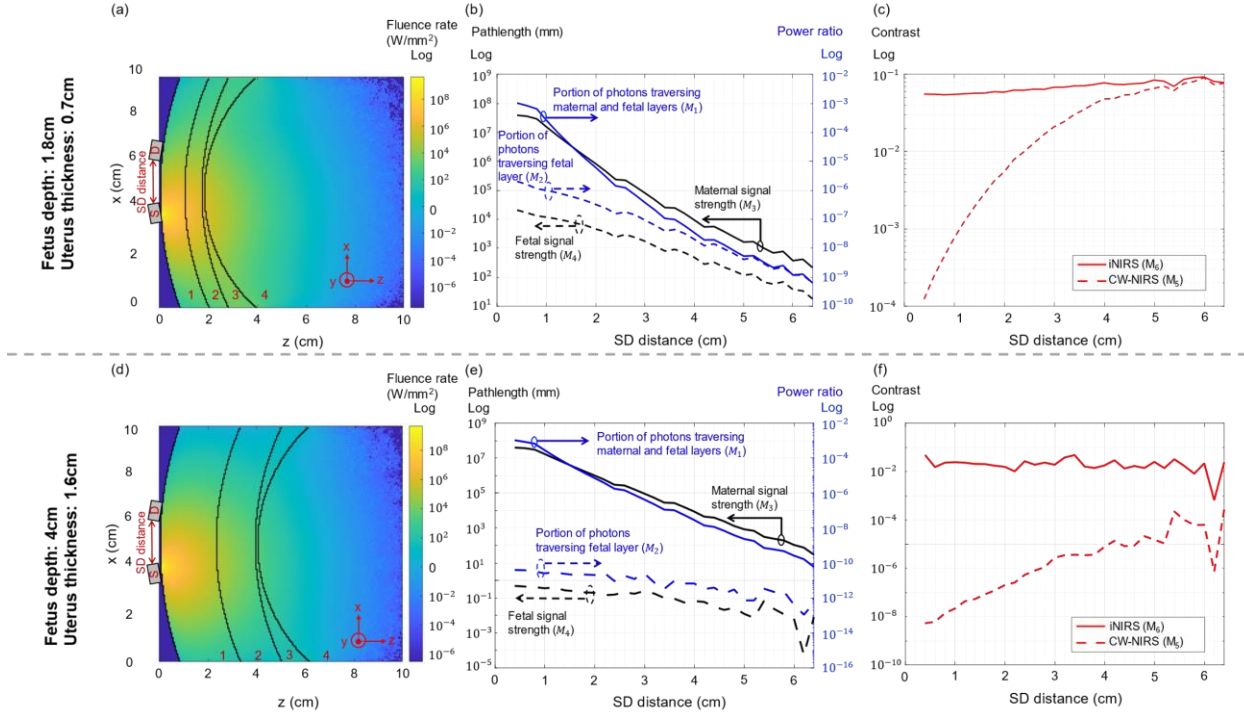


Fig. S1. (a) A cross-section view of the 3D tissue model used in the Monte Carlo simulations. The model was constructed based on the pregnant human which consists of four spherical regions (Table 1 in the main article) and was rotationally symmetry along axis $x = 5$ cm. The source (S) and detector (D) were positioned at the surface of layer 1, symmetrically along axis $x = 5$ cm. The fetal depth was 1.8 cm and the uterus thickness was 0.7 cm. (b) The evaluated metrics ($M_1 \sim M_4$) for SD distance ranging from 0~6.4 cm. (c) The fetal signal contrast of CW-NIRS (M_5) and iNIRS (M_6) for different SD distances. (d-f) Same as (a)-(c), but with 4 cm fetal depth and 1.6 cm uterus thickness.

2. Experimental setup of iNIRS

We implemented a portable, fiber-optics-based iNIRS system (Fig. 2a in the main article). We used a distributed feedback (DFB) laser [4] (Eagleyard EYP-DFB-0852-00100-1500-BFW01-0002) as the light source, with a central wavelength $\lambda_c = 851$ nm and a static linewidth of 2 MHz. We modulated the laser's wavelength/optical frequency through its current at 100 Hz sinusoidally. The output collimated beam passed through a 55 dB optical isolator (Thorlabs IOT-5-850-VLP), and was coupled to a single mode fiber (Thorlabs 780HP, 0.13 NA). The light was then split into 99% to the sample arm and 1% to the reference arm through a 99/1 fiber coupler. Light from the sample arm was collimated and illuminated on the sample, with an average power of ~ 50 mW and a spot size of 4 mm. Such an intensity is below the American National Standards Institute maximum permissible exposure of 4 mW/mm². The diffusive light reflected from the tissue was collected by a collection fiber located at a certain distance away from the illumination spot. The collected light was then combined with that from the reference arm through a 50/50 fiber coupler. A polarization controller was used to adjust the light polarization at the reference arm so as to maximize the light interference signal of the two paths. The interference signal was detected by a balanced photodetector (Newport 1807-FC), which can cancel the DC signals in $I_{PD}(t)$ and obtain $I_{AC}(t)$. The signal was subsequently sampled by a digitizer at 500 kHz.

3. Principle of interferometric near-infrared spectroscopy (iNIRS)

iNIRS [5-10] shares a similar principle as the frequency-modulated continuous-wave (FMCW) method which has been widely used in radar and lidar to measure distances [11], as well as swept-source optical coherent tomography [12-14]. In iNIRS, the frequency of the laser source is modulated with a waveform. The modulated light is then separated into two beams, a reference beam, and a signal probe beam. The reference beam $a_{ref}(t)$, passing through a known distance, can be expressed as:

$$a_{ref}(t) = \eta a_0(t) = \eta |a_0(t)| e^{j\varphi(t)} \quad (S1)$$

where η is the splitting ratio of the laser light into the reference path, $|a_0(t)|$ is the instantaneous light amplitude, $\varphi(t)$ is the instantaneous phase, which could be expressed as $\varphi(t) = 2\pi \int [v_0 + \Delta v(t)] dt$, where v_0 is the nominal optical frequency of the laser and $\Delta v(t)$ is the optical frequency change due to sweeping. $v(t) = v_0 + \Delta v(t)$ denotes the instantaneous optical frequency of the laser. The signal probe beam propagates through the scattering tissue, and its output from the tissue becomes a superposition of light traveling in different paths in the tissue:

$$a_{sig}(t) = \sum_i (1 - \eta) r_i |a_0(t - \tau_i)| e^{j\varphi(t - \tau_i)} \quad (S2)$$

where r_i is the amplitude reflection factors, and τ_i is the time delay of the i^{th} path with respect to the reference beam. The reference and signal beam interferes with each other at the same detector, resulting in an interference signal:

$$I_{PD}(t) = \sigma |a_{ref}(t) + a_{sig}(t)|^2 = I_0(t) \left\{ 1 + \sum_i \left[\left| \frac{(1 - \eta)}{\eta} \beta_i(t) r_i \right|^2 + 2 \left| \frac{(1 - \eta)}{\eta} \beta_i(t) r_i \right| \cos[\varphi(t) - \varphi(t - \tau_i)] \right] \right\} \quad (S3)$$

where σ is the responsivity of the detector, $I_0(t) = \sigma |\eta a_0(t)|^2$, and $\beta_i(t) = \frac{a_0(t - \tau_i)}{a_0(t)}$. The first two terms on the right-hand side represent the DC term $I_{DC}(t) = I_0(t) [1 + \sum_i \left| \frac{(1 - \eta)}{\eta} \beta_i(t) r_i \right|^2]$. As it does not carry useful information of the photons traveling in the tissue, it can be eliminated by a high pass filter. The last term is the AC part denoted as $I_{AC}(t) = 2I_0(t) \sum_i \left| \frac{(1 - \eta)}{\eta} \beta_i(t) r_i \right| \cos[\varphi(t) - \varphi(t - \tau_i)]$. The phase difference can be simplified as $\varphi(t) - \varphi(t - \tau_i) = \tau_i (d\varphi/dt) = 2\pi v(t) \tau_i$. This AC term can then be expressed as a function of the instantaneous optical frequency $v(t)$,

$$I_{AC}(v) = 2I_0(v(t)) \sum_i \left| \frac{(1 - \eta)}{\eta} \beta_i(v(t)) r_i \right| \cos[2\pi v(t) \tau_i] \quad (S4)$$

Under the Fourier transformation, the time-resolved [or time-of-flight (TOF)] reflectance, measured as a function of delay time τ , can be obtained as:

$$I_{AC}(\tau) = \int_{v_0 - (\Delta v/2)}^{v_0 + (\Delta v/2)} I_{AC}(v) e^{-j2\pi v \tau} dv \quad (S5)$$

The broad distribution of the time-resolved reflectance indicates the signal probe beam passing through a medium with multiple scattering events which could inform the optical properties of different tissue layers.

At each cycle of the frequency sweep of the laser, we could obtain two $I_{AC}(\tau)$, corresponding to forward sweep and backward sweep. We define t_m as the duration of the forward (or backward) sweep, which is essentially the temporal resolution of the measurement. $I_{AC}(\tau)$ could thus be expressed as $I_{AC}(\tau, t)$, where $t = nt_m$ and $n = 0, 1, 2 \dots$ which represents the time index.

4. Segmentation of the time-of-flight (TOF) curve

Once we obtain the TOF curve, we could segment it to extract the signal from superficial layers (containing pure maternal signal) and deep layers (containing mixed maternal and fetal signal) in the tissue. Here we describe our procedure to find the optimized segmentation.

To maintain proper signal quality, we first define the effective TOF curve within the range between delay time τ_{start} and τ_{end} , corresponding to the delay time where the TOF intensity is one-tenth of its maximum (Fig. S2a). A TOF curve with a higher signal-to-noise ratio (SNR) could extend the effective useful range in delay. We then find the delay time (τ_0) where the TOF intensity is half of its maximum (τ_0 being larger than the delay when the TOF intensity is maximum). We note that the early segment (smaller time delay) of the TOF curve corresponds to maternal signals from the superficial layers, and we define such a segment as $[\tau_{start}, \tau_1]$. The maternal signal in the frequency power spectrum domain and time domain can be expressed as,

$$\mathcal{J}_{AC,superficial} = FT[I_{AC,superficial}(t)] \quad (S6)$$

$$I_{AC,superficial}(t) = \int_{\tau_{start}}^{\tau_1} I_{AC}(\tau, t) d\tau \quad (S7)$$

We define the SNR of the maternal signal as the ratio between the peak intensity of the heartbeat tone (typically ranging from 1~2 Hz) versus the standard deviation of the noise floor at the frequency power spectra domain. We

initialize the value of τ_1 as τ_0 . We then conduct a local maximum search to obtain the optimized τ_1 to achieve the best SNR of the maternal signal (Fig. S2b).

Next, we find the optimized segment of the TOF curve $[\tau_2, \tau_3]$ for the signal from deep tissue layer. The signal of deep tissue layer in frequency and time domain is expressed as

$$J_{AC,deep} = FT[I_{AC,deep}(t)] \quad (S8)$$

$$I_{AC,deep}(t) = \int_{\tau_2}^{\tau_3} I_{AC}(\tau, t) d\tau \quad (S9)$$

We aim to maximize the SNR of the fetal signal, which is defined as the ratio between the peak intensity of the heartbeat tone (typically ranging from 2~3 Hz) versus the standard deviation of the noise floor at the frequency power spectra domain. We initialize τ_2 as τ_0 , and τ_3 as τ_{end} . We then scan τ_2 around τ_0 and for each τ_2 , we search τ_3 to maximize the SNR of the fetal signal. This process allows us to find the best combination of τ_2 and τ_3 to achieve a global maximum of the SNR of fetal signal (Fig. S2c).

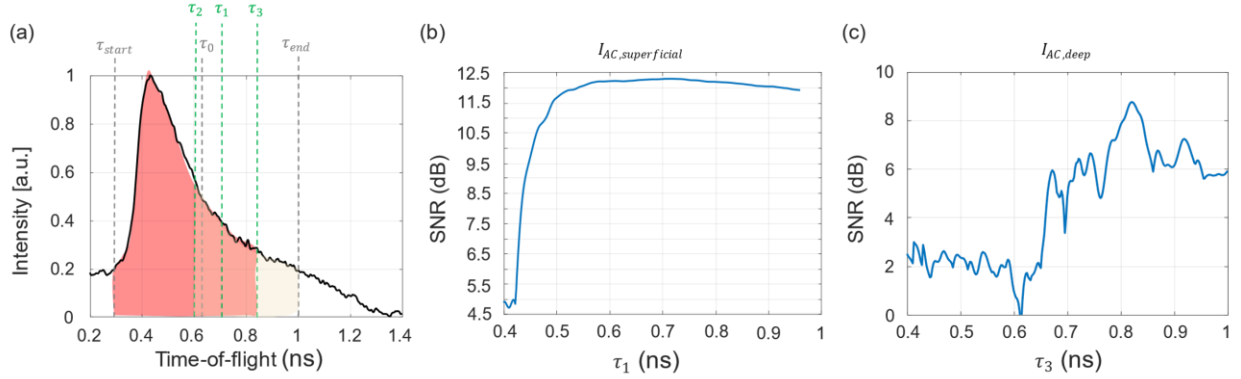


Fig. S2. (a) TOF curve with the label of τ_{start} , τ_{end} , τ_0 , τ_1 , τ_2 , τ_3 . (b) The SNR of the maternal heartbeat signal versus τ_1 . (c) The SNR of the fetal heartbeat signal versus τ_3 with $\tau_2 = 0.61$ ns. This set of data corresponds to the pregnant sheep experiment in Section 3.5 in the main article.

5. Adaptive noise cancellation method to extract pure fetal signal

The photons from the deep trajectory at the TOF contain both maternal and fetal signal. We could then use an adaptive noise cancellation algorithm [15, 16] (Fig. S3) to effectively extract the pure fetal signal by removing the maternal signal. Here, $I_{AC,deep}$ could be decomposed into fetal signal $I_{AC,deep,fetal}$ and maternal signal $I_{AC,deep,maternal}$. $I_{AC,superficial}$ contains pure maternal signal and can thus be referred as $I_{AC,superficial,maternal}$. $I_{AC,superficial,maternal}$ is correlated with $I_{AC,deep,maternal}$. The adaptive filter aims to find a value α which minimizes the power of the error signal defined as below:

$$I_{error} = I_{AC,deep,maternal} + I_{AC,deep,fetal} - \alpha I_{AC,superficial,maternal} \quad (S10)$$

Essentially, in the adaptive noise cancellation algorithm, $I_{AC,deep} = I_{AC,deep,maternal} + I_{AC,deep,fetal}$ serves as mixed signal, and $I_{AC,superficial,maternal}$ serves as noise signal, the adaptive filter aims to cancel out the maternal “noise” signal in $I_{AC,deep}$ through $I_{AC,superficial,maternal}$, thus leaving the pure signal $I_{AC,deep,fetal}$.

The expectation of I_{error}^2 in Eq. S10 is written as:

$$E\{I_{error}^2\} = E\{I_{AC,deep,fetal}^2\} + E\{(I_{AC,deep,maternal} - \alpha I_{AC,superficial,maternal})^2\} + 2E\{I_{AC,deep,fetal}(I_{AC,deep,maternal} - \alpha I_{AC,superficial,maternal})\}, \quad (S11)$$

If $I_{AC,deep,maternal}$ is uncorrelated to $I_{AC,deep,fetal}$, which satisfies the condition in the pregnant model, we have $E\{I_{AC,deep,fetal}(I_{AC,deep,maternal} - \alpha I_{AC,superficial,maternal})\} = 0$. Eq. S11 is then simplified as:

$$E\{I_{error}^2\} = E\{I_{AC,deep,fetal}^2\} + E\{(I_{AC,deep,maternal} - \alpha I_{AC,superficial,maternal})^2\}. \quad (S12)$$

We can then find the value of α by solving the problem to minimize $E\{I_{error}^2\}$ through recursive least square (RLS) algorithm,

$$\min_{\alpha} E\{I_{AC,deep,fetal}^2\} + E\{(I_{AC,deep,maternal} - \alpha I_{AC,superficial,maternal})^2\}. \quad (S13)$$

The iterations of minimizing $E\{I_{error}^2\}$ stop as the output of the adaptive filter $\alpha I_{AC,superficial,maternal}$ is as similar as $I_{AC,deep,maternal}$ and leads to the $I_{error} \approx I_{AC,deep,fetal}$.

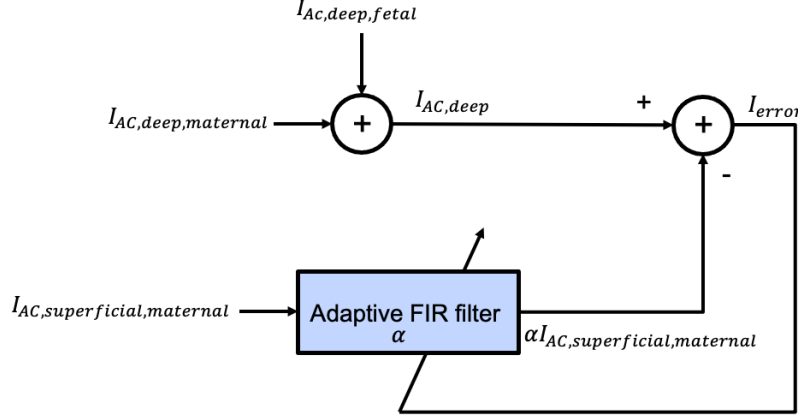


Fig. S3. Block diagram of the adaptive noise cancelling algorithm.

6. Estimation of oxygen saturation

$I_{AC,deep,fetal}$ is modulated by the cardiac cycle of the fetus. At the systolic phase, there are larger volume of both oxygenated and deoxygenated hemoglobin in the arteries, causing higher light absorption and thus a smaller $I_{AC,deep,fetal}$. The opposite happens at diastolic phase. Using the modified Beer-Lambert law, we can relate the ratio of $I_{AC,deep,fetal}$ between the systolic and diastolic phase with the change of light absorption coefficient of the tissue:

$$\Delta A_{AC,deep,fetal} = -\ln\left(\frac{I_{AC,deep,fetal,systole}}{I_{AC,deep,fetal,diastole}}\right) = \Delta\mu_{a,fetal} \times \left\langle \sum_{k \in \{N_M+F\}} L_k^f \right\rangle \quad (S14)$$

where $\Delta\mu_{a,fetal}$ is the change of the absorption coefficient of the fetal tissues during a cardiac cycle, and $\langle \sum_{k \in \{N_M+F\}} L_k^f \rangle$ is the mean pathlength in the fetal layer for photons traversing the deep layer (i.e. both the maternal and fetal tissues).

$\Delta\mu_{a,fetal}$ is mainly contributed by the concentration change of two chromophores: oxyhemoglobin (HbO_2) and deoxyhemoglobin (Hb) during a cardiac cycle. The arterial oxygen saturation SpO_2 for pulse oximetry is defined as: $SpO_2 = \frac{[HbO_2]}{[HbO_2] + [Hb]} \times 100\%$, where $[HbO_2]$ and $[Hb]$ is the concentration of HbO_2 and Hb in the arteries respectively. By performing the same measurement of $\Delta\mu_{a,fetal}$ through two optical wavelengths λ_1 and λ_2 , we could solve SpO_2 through the following expressions:

$$\begin{aligned} R = \frac{\Delta A_{AC,deep,fetal}^{\lambda_1}}{\Delta A_{AC,deep,fetal}^{\lambda_2}} &= \frac{-\ln\left(\frac{I_{AC,deep,fetal,systole}^{\lambda_1}}{I_{AC,deep,fetal,diastole}^{\lambda_1}}\right)}{-\ln\left(\frac{I_{AC,deep,fetal,systole}^{\lambda_2}}{I_{AC,deep,fetal,diastole}^{\lambda_2}}\right)} \\ &= \frac{\ln(10)(\epsilon_{HbO_2,\lambda_1} \Delta[HbO_2] + \epsilon_{Hb,\lambda_1} \Delta[Hb]) \langle \sum_{k \in \{N_M+F\}} L_k^f \rangle_{\lambda_1}}{\ln(10)(\epsilon_{HbO_2,\lambda_2} \Delta[HbO_2] + \epsilon_{Hb,\lambda_2} \Delta[Hb]) \langle \sum_{k \in \{N_M+F\}} L_k^f \rangle_{\lambda_2}} \quad (S15) \end{aligned}$$

$$SpO_2 = \frac{\epsilon_{Hb,\lambda_2} R \left(\frac{\langle \sum_{k \in \{N_M+F\}} L_k^f \rangle_{\lambda_2}}{\langle \sum_{k \in \{N_M+F\}} L_k^f \rangle_{\lambda_1}} \right) - \epsilon_{Hb,\lambda_1}}{(\epsilon_{HbO_2,\lambda_1} - \epsilon_{Hb,\lambda_1}) - R \left(\frac{\langle \sum_{k \in \{N_M+F\}} L_k^f \rangle_{\lambda_2}}{\langle \sum_{k \in \{N_M+F\}} L_k^f \rangle_{\lambda_1}} \right) (\epsilon_{HbO_2,\lambda_2} - \epsilon_{Hb,\lambda_2})}. \quad (S16)$$

where $\epsilon_{HbO_2,\lambda}$ and $\epsilon_{Hb,\lambda}$ is the known molar extinction coefficient of oxyhemoglobin and deoxyhemoglobin at the optical wavelength λ .

In the experiment reported in this paper, our major goal was to validate if the iNIRS could collect the photons traversing in the fetal layer in the deep tissue and recover $I_{AC,deep,fetal}$. Our experiment setup thus only contained a single laser.

7. Thermally expanding core (TEC) fiber for photons collection

7.1 Geometry of the thermally expanding core (TEC) fiber

In typical iNIRS, the collection fiber is a single mode fiber, which has a small collection efficiency. Optimizing the design of the collection optics could boost the number of captured photons and thus facilitate the measurement of signals from deep tissue. Here, we innovatively use a mode-field adaptor (MFA) to increase the collection efficiency of the diffused light into the fundamental mode of a single-mode fiber (SMF). It is important that the light could be converted to the fundamental mode of the SMF so that it could interfere with the signal from the reference arm (which is composed of an SMF) to obtain the TOF curve.

The MFA is a fiber device that expands the mode field of an SMF into the fundamental mode field of a large-mode area (LMA) fiber, which is typically a multi-mode fiber (MMF), with a minimum insertion/conversion loss. If one directly connects the SMF and LMA, the insertion/conversion loss can be expressed as

$$\alpha = -20 \log \frac{2\omega_{SMF} \times \omega_{LMA}}{\omega_{SMF}^2 + \omega_{LMA}^2} \quad (S17)$$

where ω_{SMF} is the mode-field diameter (MFD) of SMF and ω_{LMA} is the mode-field diameter of LMA. Compared with LMA, the MFD of SMF is very small, which could lead to a high mode field mismatch loss and thus a large α . In MFA, the core of the SMF is thermally expanded into the core of the LMF. The mode field of SMF thus gradually expands to that of LMA and thus α is decreased. The schematics of a thermally expanding core (TEC) fiber is illustrated in Fig. S4. The core radius a of the SMF with cladding radius R is thermally expanded to core radius A , which matches that of LMA fiber. The expanding region of the fiber is much longer than the radial size of the SMF, and thus, the core can be considered uniformly expanded. When the SMF is heated, the dopants of the core will diffuse to the cladding. As a result, the refractive index of the core decreases and the effective core radius increases. The fundamental mode of the SMF could be gradually converted to that of the LMA fiber, without exciting high-order modes.

Here, we use the MFA with light propagation opposite to the conventional direction. The diffused light emitted from the tissue surface is collected through an MMF, which is connected to the MFA, followed by an SMF. We term this as a compound collection fiber. Compared with a pure SMF, the compound collection fiber is able to collect more light and output a strong light intensity in the fundamental mode of the SMF. This is supported by the numerical simulation (Sec. 2.3 and 3.2 in the main article, and Supplementary Information Sec. 7.2) and experiment (Sec. 2.4 and 3.3 in the main manuscript).

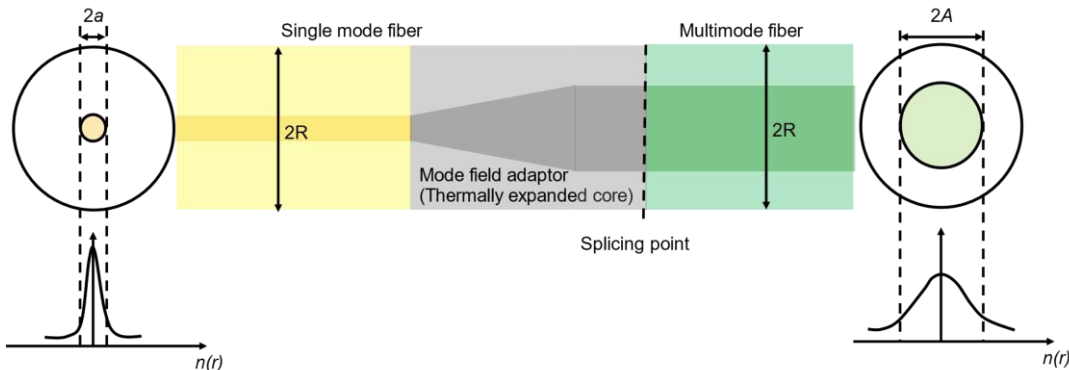


Fig. S4. Schematic of a thermally expanded core fiber. The single mode fiber and multimode fiber has a core diameter of $2a$ and $2A$ respectively. Both of fibers have a diameter of $2R$. $n(r)$ illustrates the refractive index profile of the fiber.

7.2 Numerical simulation of diffused light coupling into SMF or the compound collection fiber

Here we describe the numerical simulation to study the light collection efficiency through a pure SMF or the compound collection fiber. There are two steps in this simulation: first construct the electrical field mimicking that at the tissue surface, and then propagate this field through the SMF or compound collection fiber and detect the power at the end of the fiber.

We first constructed the electrical field at the tissue surface, whose intensity appears to be a speckle pattern due to the multiple scattering events of the laser light in the tissue. We synthesized the complex amplitude of the speckle pattern through the summation of guided modes supported by the MMF. The guided modes of a step-index MMF are determined by its V number, which is a function of the numerical aperture (NA), fiber core radius, and operating wavelength. It starts with solving the wave equation in cylindrical symmetry with the step-index fiber boundary condition. The general solutions in the core and cladding regions are given as the first kind and second kind of m^{th} order Bessel function with propagation constant β . For a given set of parameters such as wave number (k_0), core radius, core refractive index, and cladding refractive index, the eigenvalue equation can be solved numerically to determine the propagation constant β for different orders of m . In general, there may be multiple solutions for each m , which can be denoted as β_{mn} . Each β_{mn} presents one possible linearly polarized (LP) mode propagation in the fiber. The spatial distribution of transverse electrical field for an LP mode is then described by a piece-wise combination of Bessel functions [17] in the core and cladding region. The complex amplitude (i.e. electrical field) of the speckle pattern could then be synthesized by summing all the spatial modes having independent complex amplitude with real and imaginary parts that are zero mean, independent, and identically distributed in a 2D Gaussian distribution.

We then used the complex speckle pattern as the input of the pure SMF or compound fiber, and a Finite Difference Beam Propagation Method (FD-BPM) [18] to simulate light propagation in the fiber. The FD-BPM uses the Douglas-Gunn Alternating Direction Implicit method to solve the beam propagation and could model light propagation in a wide variety of optical fiber geometries with arbitrary refractive index profile. The compound fiber is modeled as a sequential connection of 1 cm of MMF, 6 cm of MFA and, 24 cm of SMF, thus 31 cm in total length. The core diameter of the MFA shrinks uniformly from that of the MMF to the SMF. For the pure SMF case, we set it as 31 cm in length in the simulation. We launched the same complex speckle pattern to both the pure SMF and the compound fiber. As the light propagates, the modes that are not guided by the fiber radiate out and thus the power remaining in the fiber of interest drops. Eventually, the light field converges to that of the fundamental mode in the SMF and optical power stays stable.

In our experiment, we used an MMF with an NA of 0.22, core/cladding diameter of 105 μm /125 μm , and 851 nm laser light, resulting in a V number of 85.277. The number of guided modes of the MMF is then estimated as $M \approx V^2/2=3636$. The speckle patterns are thus synthesized by these 3636 modes. We compared the optical power (normalized to the input power) at the end of both fibers, for a total of 20 independently generated speckle patterns, formed by summing the spatial modes with different complex weights (Fig. S5). On average, the collection efficiency increases by $\sim 3.6\times$ for the compound fiber.

To remove any potential bias, we also calculated the guided modes of the MMF using an MMF that could support more modes (thus a larger NA, which could support 5000 modes) than the one used in our experiment, and we used these modes (5000 in total) to synthesize the complex amplitude of the speckle pattern. We propagated the speckle pattern through the same compound fiber and pure SMF as above. The comparison results are shown in the main article Fig. 4. On average, the collection efficiency increases by $\sim 3.4\times$ for the compound fiber, comparable with the results ($\sim 3.6\times$) using 3636 modes.

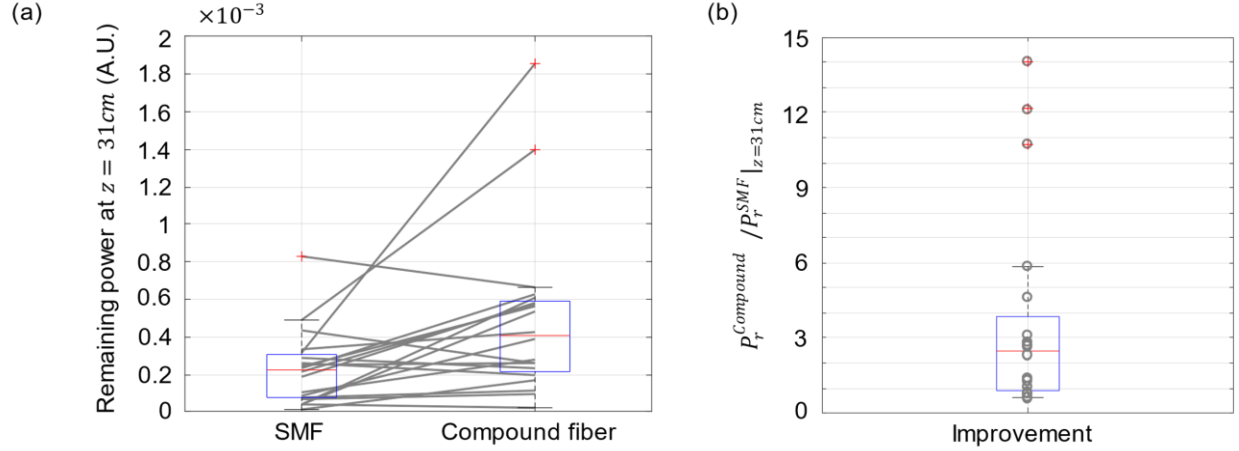


Fig. S5. (a) The remaining power at the SMF and compound fiber after light from the speckle patterns (synthesized from 3636 modes of the MMF) couples into and propagates 31 cm through the fiber. A total of 20 independently generated speckle patterns were tested. (b) The ratio of the remaining power at compound fiber versus the SMF at $z = 31 \text{ cm}$, for 20 different speckle patterns. The boxplot summarizes the data statistically. Center bars (red), medians; box edges, first and third quartiles, respectively; whiskers, minimum and maximum; + mark, outlier. The 20 speckle patterns were formed by superimposing spatial modes with 20 different sets of complex mode coefficients drawn from the 2D Gaussian distribution. $z = 31 \text{ cm}$ was the exit of both SMF and compound fiber.

8. Measurement details in iNIRS experiments of fluid phantom samples

For the fluid phantom samples experiments, the iNIRS was set up as the transmission mode. We first aligned the source and detector without inserting the fluid phantom in order to ensure the maximum power was received. For each sample, 24,000 consecutive interference signals from the forward and backward laser sweeping were collected at the laser sweep rate of 100 Hz within 2 minutes. The time-domain interference fringe patterns and the TOF curves were extracted for each measurement time stamp. As the sample can be considered as quasi-static, we averaged all the TOF curves to increase the signal-to-noise ratio (SNR).

9. Extraction of the optical properties of phantom samples by fitting the TOF curve with radiative transfer equation

The optical properties of the sample (such as the absorption coefficient μ_a and the reduced scattering coefficient μ'_s) could be extracted by fitting the TOF curve measured by iNIRS to the Radiative Transfer Equation (RTE) for the fluence rate under the diffusion approximation. The fitting procedure involves nonlinear optimization and is carried out by minimizing the squared norm of the difference between the transmittance predicted by the diffusion theory ($I_{AC}^{(DE)}(\tau)$) [5] and the actual experimental data ($I_{AC}^{(iNIRS)}(\tau)$). This optimization problem can be defined as below:

$$\min_{\mu_a, \mu'_s} \left\| \log[I_{AC}^{(DE)}(\tau) * I_0(\tau)] - \log[\alpha I_{AC}^{(iNIRS)}(\tau)] \right\|^2, \quad (S18)$$

where $I_0(\tau)$ is the system instrument response function (IRF), which is measured through putting an air gap between the source and detector under the transmission scheme, * represents the convolution, and α is a normalization factor for the measured intensity. The absorption coefficient plays a critical role in determining the slope of the TOF for larger values of τ [5]. To account for this relationship, the optimization procedure described in Eq. (S18) is carried out on a logarithmic scale.

10. Protocol of experiment on the pregnant sheep

The study was evaluated and approved by the UC Davis Institutional Animal Care and Use Committee (IACUC) and the care for the animals complied with the guidelines set by the Guide for the Care and Use of Laboratory Animals. A pregnant sheep near term (136 days of gestation) was anesthetized. Vertical laparotomy and hysterotomy were subsequently made to expose the fetus. An arterial blood line was inserted in the fetus' carotid artery for precise and continuous hemodynamic monitoring and accessed for fetal blood sampling. After replacing the lost amniotic fluid

with warm saline, the exposed fetus was returned to the uterus. To create a deterministic tissue geometry for identifying the location of the fetus, one ear of the lamb was sutured to the ewe's uterine wall. The incisions were then closed. A transabdominal model was built for measurement. The conventional pulse oximetry was clipped onto the maternal ewe's abdominal wall at the laparotomy site to capture the maternal heart rate (MHR). The monitored vital signs (MHR, FHR [fetal heart rate]) were logged through BIOPAC. The maternal and fetal heartbeat measuring from the conventional pulse oximetry and hemodynamic monitor, respectively, were the ground truth for the comparison against our transabdominal approach. The source and detector probe of the iNIRS setup was put on the maternal abdomen above the underlying fetus. An illustration of the fetal sheep model setup can be seen in Fig. 8(a) in the main article.

References

1. P. L. Carson, J. M. Rubin, and E. H. Chiang, "Fetal depth and ultrasound path lengths through overlying tissues," *Ultrasound Med Biol* **15**, 629-39 (1989).
2. S. Degani, Z. Leibovitz, I. Shapiro, R. Gonen, and G. Ohel, "Myometrial thickness in pregnancy: longitudinal sonographic study," *J Ultrasound Med* **17**, 661-665 (1998).
3. P. Kovacs, S. Matyas, K. Boda, and S. G. Kaali, "The effect of endometrial thickness on IVF/ICSI outcome," *Human Reproduction* **18**, 2337-2341 (2003).
4. H. Kogelnik and C. V. Shank, "Coupled-wave theory of distributed feedback lasers," *J. Appl. Phys.* **43**, 2327–2335 (1972).
5. D. Borycki, O. Kholiqov, S. P. Chong, and V. J. Srinivasan, "Interferometric Near-Infrared Spectroscopy (iNIRS) for determination of optical and dynamical properties of turbid media," *Optics Express* **24**, 329-354 (2016).
6. D. Borycki, O. Kholiqov, and V. J. Srinivasan, "Interferometric near-infrared spectroscopy directly quantifies optical field dynamics in turbid media," *Optica* **3**, 1471-1476 (2016).
7. O. Kholiqov, D. Borycki, and V. J. Srinivasan, "Interferometric near-infrared spectroscopy (iNIRS): performance tradeoffs and optimization," *Optics Express* **25**, 28567-28589 (2017).
8. O. Kholiqov, W. Zhou, T. Zhang, V. N. D. Le, and V. J. Srinivasan, "Time-of-flight resolved light field fluctuations reveal deep human tissue physiology," *Nature Communications* **11**, 391 (2020).
9. L. Mei, G. Somesfalean, and S. Svanberg, "Frequency-modulated light scattering interferometry employed for optical properties and dynamics studies of turbid media," *Biomed. Opt. Express* **5**, 2810-2822 (2014).
10. J. M. Tualle, H. L. Nghiêm, M. Cheikh, D. Etori, E. Tinet, and S. Avrillier, "Time-resolved diffusing wave spectroscopy beyond 300 transport mean free paths," *J. Opt. Soc. Am. A* **23**, 1452-1457 (2006).
11. L. Piotrowsky, T. Jaeschke, S. Kueppers, J. Siska, and N. Pohl, "Enabling High Accuracy Distance Measurements With FMCW Radar Sensors," *IEEE Transactions on Microwave Theory and Techniques* **67**, 5360-5371 (2019).
12. U. Glombitza and E. Brinkmeyer, "Coherent frequency-domain reflectometry for characterization of single-mode integrated-optical waveguides," *Journal of Lightwave Technology* **11**, 1377-1384 (1993).
13. S. Chen, B. Potsaid, Y. Li, J. Lin, Y. Hwang, E. M. Moul, J. Zhang, D. Huang, and J. G. Fujimoto, "High speed, long range, deep penetration swept source OCT for structural and angiographic imaging of the anterior eye," *Scientific Reports* **12** (2022).
14. R. Huber, M. Wojtkowski, K. Taira, J. Fujimoto, and K. Hsu, "Amplified, frequency swept lasers for frequency domain reflectometry and OCT imaging: design and scaling principles," *Opt Express* **13**, 3513-28 (2005).
15. E. Zahedi and G. K. Beng, "Applicability of adaptive noise cancellation to fetal heart rate detection using photoplethysmography," *Comput Biol Med* **38**, 31-41 (2008).
16. D. D. Fong, K. J. Yamashiro, K. Vali, L. A. Galganski, J. Thies, R. Moeinzadeh, C. Pivetti, A. Knoesen, V. J. Srinivasan, H. L. Hedriana, D. L. Farmer, M. A. Johnson, S. Ghiasi, "Design and In Vivo Evaluation of a Non-Invasive Transabdominal Fetal Pulse Oximeter," *IEEE Transactions on Biomedical Engineering* **68**, 256-266 (2021).
17. C.-L. Chen, *Foundations for Guided-Wave Optics*. John Wiley & Sons, Inc., 2006.
18. M. Veetikazhy, A. Kragh Hansen, D. Marti, S. Mark Jensen, A. Lykke Borre, E. Ravn Andresen, K. Dholakia, and P. Eskil Andersen, "BPM-Matlab: an open-source optical propagation simulation tool in MATLAB," *Optics Express* **29**, 11819-11832 (2021).